Supplementary Note 1. Modeling of light attenuation and curing depth in frontal photopolymerization (FPP)

Vitale et al. developed a theoretical model to describe the curing kinetics of frontal photopolymerization (FPP) [1]. In this model, the reaction conversions rate $\frac{\partial\phi(z,t)}{\partial t}$, is proportional to both the local light intensity $I(z,t)$ and the concentration of unreacted monomers, as is given by:

$$\frac{\partial\phi(z,t)}{\partial t} = K[1-\phi(z,t)]I(z,t), \tag{1}$$

where K is the photopolymerization reaction rate constant. The attenuation of light through the thickness direction follows a two-component Beer-Lambert law:

$$\frac{\partial I(z,t)}{\partial z} = -\bar{\mu}(z,t)I(z,t), \tag{2}$$

where I is the light intensity, z is the coordinate in the thickness direction, $\bar{\mu}$ is the effective attenuation coefficient, and t is irradiation time.

As shown in Fig. S3, the cured thickness exhibits a logarithmic dependence on the UV dose with a constant of proportionality of $1/\mu$, corresponding to photoinvariant polymerization conditions. Under this assumption, the conversion profile is given by:

$$\phi(z,t) = 1-\exp[-KI_0\exp(-\mu z)\,t] \tag{3}$$

and the position of the polymerization front, which defines the cured depth z, is given by:

$$z = \frac{\ln\left[\frac{KI_0t}{\ln\left(\frac{1}{1-\phi_c}\right)}\right]}{\mu} = \frac{\ln(I_0t)}{\mu} - \frac{\ln\left[\frac{\ln(1/1-\phi_c)}{K}\right]}{\mu}, \tag{4}$$

where the ϕ_c is the critical normalized conversion at gelation.

Therefore, the cured depth as a function of light dose (I_0t), shown in Fig. S3, is fitted using Eq. S4, yielding attenuation coefficients of $\mu_{0\,\mathrm{wt\%}} = 1.162\ \mathrm{mm}^{-1}$ and $\mu_{0.02\,\mathrm{wt\%}} = 1.986\ \mathrm{mm}^{-1}$.

Supplementary Note 2. Determination of critical normalized conversion (ϕ_c) and kinetic constant *K*

The degree of conversion (χ), is determined from the relative absorbance peak intensity in FTIR spectra [2, 3]. The absorbance of the vinyl C=C bond at 810 cm^{-1} (I_{810}) is normalized by that of the aromatic *sp*^{2} C-H band at 840 cm^{-1} (I_{840}). The degree of conversion (DoC) is then calculated as:

$$\chi = 1 - \frac{I_{810}/I_{840}}{[I_{810}/I_{840}]_{t=o}}, \tag{5}$$

As shown in Fig. S4A, the FTIR spectrum of resin solution yields $(I_{810}/I_{840})_{t=0} = 9.22$. Fig. S4B shows the FTIR spectra of the polymer at the critical gel point, from which a critical conversion rate $\chi_{\mathrm{c}} = 0.445$ is obtained. The extent of polymerization, $\phi(z,t)$, is defined as the normalized conversion and is given by:

$$\phi(z,t) = \chi(z,t)/\chi_{\max}\,. \tag{6}$$

Here, $\chi_{\max} = 0.99$ is determined from the fully cured resin (Fig. S4C) and substituting χ_{c} into Eq. S6 gives $\phi_{\mathrm{c}} = 0.445$. Substituting ϕ_{c} into Eq. (4) allows the reaction kinetic constant *K* to be extracted by fitting the curing-depth data in Fig. S3, yielding *K* = 0.00316 cm^2·mW^{-1}·s^{-1} for resins containing 0.02 wt% Sudan I, respectively. Using the obtained *K*, ϕ_{c}, and $\mu_{0.02\ \mathrm{wt\%}}$, Eq. S3 is then used to obtain the relationship between normalized conversion and sample depth, as shown by the dashed line in Fig. 2C.

Supplementary Note 3. Validation of equivalence between thin-film samples and GMA

To determine the modulus distribution within the GMA, the Beer-Lambert law is used to calculate the local light intensity at different depths (*z* = 0, 0.2, 0.4, 0.6, 0.8, 1 mm). Thin-film specimens with a thickness of 150 μm are then prepared under the corresponding light intensities and subjected to tensile testing to obtain the effective Young's modulus at each depth. This approach preserves the same light intensity experienced locally within GMA, ensuring that the thin films reproduce the mechanical properties of the corresponding regions within the GMA (Fig. S5).

According to Eq. S3, the conversion at two arbitrary positions z_1 and z_2 in the GMA is given by:

$$\phi_1 = 1 - \exp(-KI_0 \exp(-\mu z_1)\, t)\,, \phi_2 = 1 - \exp(-KI_0 \exp(-\mu z_2)\, t) \tag{7}$$

The incremental conversion between these two positions is obtained by:

$$\Delta\phi = \exp(-KI_0 \exp(-\mu z_1)\, t) - \exp(-KI_0 \exp(-\mu z_2)\, t) \tag{8}$$

For the thin-film specimens cured under a uniform incident intensity I_0', the corresponding incremental conversion is:

$$\Delta\phi' = \exp(-KI_0' \exp(-\mu z_1')\, t) - \exp(-KI_0' \exp(-\mu z_2')\, t) \tag{9}$$

By setting the incident intensity for the thin film equal to the local intensity at depth z1 in the GMA, $I_0' = I_1 = I_0 \exp(-\mu z_1)$, the same initial conversion level is referenced, such that $\phi_1' = \phi_1$. Under this condition, Eq. S9 reduces to:

$$\Delta\phi' = \exp(-KI_0 \exp(-\mu z_1)\, t) - \exp(-KI_0 \exp(-\mu z_2)\, t) = \Delta\phi \tag{10}$$

This result demonstrates that the thin-film specimens cured under depth-matched irradiation reproduce the same conversion distribution as the corresponding regions within the GMA, thereby validating their equivalence.

Supplementary Note 4. Pull-off tests for characterizing size and shape effects onadhesion

GMA and control groups with radii *R* = 0.5, 1, 2, 3, 4, 5, 10, 20 mm and with various shapes (circular, decagonal, octagonal, hexagonal, square, triangular, and star-shaped) are fabricated by laser cutting (Fig S7). Pull-off tests are then performed to measure the adhesion strength, with the experimentally setup and measurement procedures shown in Fig. S8A. During testing, each sample is brought into contact with the glass substrate at a speed of 10 µm/s until a prescribed preload is applied, held for 2 min, and then retracted at 100 µm/s. To determine an appropriate preload, tests were conducted under progressively increasing preload values (GMA: 10 - 50 N; PDMS: 5 - 20 N; Ecoflex: 1 - 10 N) until the pull-off force reached a teady plateau, indicating the establishment of conformal contact (Fig. S5B-E). Adhesion strength was calculated as the pull-off force divided by the contact area. For the GMA, adhesion tests under both load- and displacement-controlled conditions show that load control requires a lower applied force to reach saturation; however, once conformal contact is established, the measured adhesion strength is identical under both control modes.

Supplementary Note 5. Finite-element simulations for the size effect on adhesion

Two-dimensional finite-element analysis (FEA) is performed in ABAQUS to explore the detach behavior of GMA, PDMS, Ecoflex over a wide range of radii from

100 μm to 10 mm, with a fixed sample thickness of 1 mm. An axisymmetric model is used for simplifying this 3D geometry. Because of the large modulus contrast between the glass plate and soft adhesives, the glass plate is modelled as a rigid body. PDMS and Ecoflex are described using a neo-Hookean hyperplastic model to capture their nonlinear deformation during detachment, with parameters obtained from tensile tests: $\mu_{PDMS} = 2$ MPa, $D_{PDMS} = 0.104$ MPa^{-1}, $\rho_{PDMS} = 970$ kg/m^3, $\mu_{Ecoflex} = 0.5$ MPa, $D_{Ecoflex} = 0.414$ MPa^{-1}, $\rho_{Ecoflex} = 1040$ kg/m^3. For the GMA, the experimentally measured Young's modulus gradient along the thickness direction (raising from 2MPa to 170MPa, as shown in Fig. 2F) is implemented thorugh a field-dependent modulus using the USDFLD subroutine. The Poisson's ratio of GMA is set to 0.45, and the density was taken as 1000 kg/m^3.

The detachment process is simulated by imposing a vertical displacement on the top surface using a quasi-static explicit procedure. The top surfaces is retracted at a constant velocity of 0.1 mm·s^{-1}, while the bottom surface of each adhesives is assumed to be fully bonded to the glass plate through a thin cohesive layer with a thickness of 0.1 μm. The cohesive elements are defined by a bilinear traction-separation law with parameters: $G_{PDMS} = 1$ J/m^2, $\sigma_{PDMS} = 0.4$ MPa [4], $G_{Ecoflex} = 0.5$ J/m^2, $\sigma_{Ecoflex} = 0.1$ MPa [4] and $G_{GMA} = 700$ J/m^2, $\sigma_{GMA} = 1.2$ MPa (mearsured by 90 degree peeling test, as in Fig. S11). Four-node axisymmetric elements (CAX4R) and cohesive elements (COHAX4) are used for the bulk materials and the interfacial layers, respectively.

As the radius increase from 0.1 mm to 5 mm, GMA maintains a nearly uniform interfacial stress distribution, whereas PDMS and Ecoflex progressively develop pronounced edge-localized stress concentrations (Fig. S12).

Supplementary Note 6. FEA simulation for the shape-effect on adhesion

3D FEA simulations are performed in ABAQUS to model the detachment of adhesives with square, star and circular shapes of equal area and a fixed thickness of 1 mm. The same materials properties as described above are used.

The detachment process is simulated by imposing displacement boundary conditions under quasi-static explicit procedures. The top surfaces are displaced vertically at a constant velocity of 0.1 mm·s^{-1}, while the bottom surface are bonded to a rigid glass plate through a thin cohesive layer with a thickness of 0.1 μm, defined using the same bilinear traction-separation parameters as in Section S5. Eight-node brick elements (C3D8) and cohesive elements (COH3D8) are used for the bulk materials and interfacial layers, respectively.

Supplementary Note 7. Pull-off test on rough surfaces

As surface roughness increases (Fig. S13), a higher preload is required to achieve conformal contact. To quantify this effect, adhesion tests are performed under the same conditions as for smooth surface (Supplementary Note 4) but with varying preload levels (Fig. S14-16). The results show that adhesion strength increases with preload and reaches a plateau once conformal contact is established. Ecoflex, owing to its low modulus, adhered readily to rough surfaces. By contrast, the GMA, whose modulus at the contact interface is comparable to that of PDMS, requires larger preloads to achieve full contact. However, whereas PDMS rapidly loses adhesion on rough surfaces because of stress concentrations at surface asperities, the GMA maintains strong adhesion as its graded modulus design redistributes interfacial stresses and suppresses asperity-induced stress concentrations.

Supplementary Note 8. FEA simulation for the thermally switchable adhesion of GMA

The USDFLD subroutine is used to implement the temperature-dependent material properties of the GMA. As shown in Fig. 2F, distinct Young’s modulus profiles along the thickness direction are prescribed at room temperature and at 80 °C. In the USDFLD implementation, the Young’s modulus of GMA is defined as a field-dependent variable associated with a user-defined field. For simplicity, the Young’s modulus is set equal to the value of this field.

To capture the spatial distribution, the Eulerian coordinates of each integration point are extracted, and the local thickness is mapped onto the z-axis coordinates. On this basis, two field-dependent modulus profiles are defined to represent the material properties at the two temperatures. To enable thermal switching, the temperature field is also accessed within the USDFLD subroutine, and a simple criterion ($T < 80$ °C or $T \geq 80$ °C) is used to select the appropriate modulus profiles.

If a smoother transition is desired, the Young's modulus can alternatively be prescribed as a continuous function of both thickness and temperature.

Supplementary Note 9. Comparison between the GMA and commercial tapes

All tests are conducted to benchmark the GMA against several widely used commercial double-sided tapes under a low preload of 30 N and a short contact time of 2 min. These constraints are chosen to reflect practical applications scenarios in which adhesives are expected to operate under rapid handling, moderate pressure and limited contact time. Although commercial tapes show modest improvements on rough surfaces owing to their compliance, their adhesion strengths remained substantially lower than those of the GMA, which achieved 635 kPa on rough surfaces and 710 kPa on PTFE.

Moreover, commercial tapes exhibit limited adaptability to non-ideal geometries, lacked tunable adhesion control, and show poor durability under sustained static loads. By contrast, the GMA maintains robust adhesion across complex geometries, enabled thermally triggered reversible adhesion, and substantially extends adhesion lifetime under static loading. Detailed comparison data are provided in Table S2.

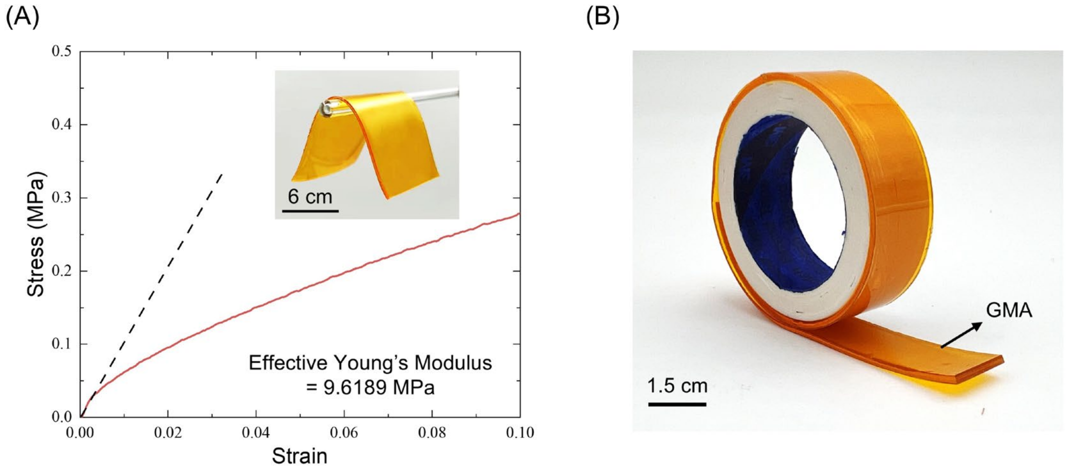

Fig. S1 (A) Strain-stress curve of 1 mm GMA used to calculate its effective Young's modulus and demonstrate its compliance. (B) GMA fabricated into roll-to-toll format, highlighting scalable manufacturability and compatibility with tape-like applications.

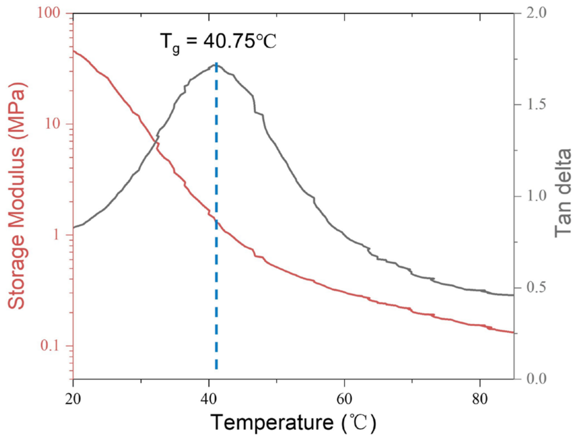

Fig. S2 Storage modulus and loss modulus??? of the GMA at different temperatures, obtained from DMA tests.

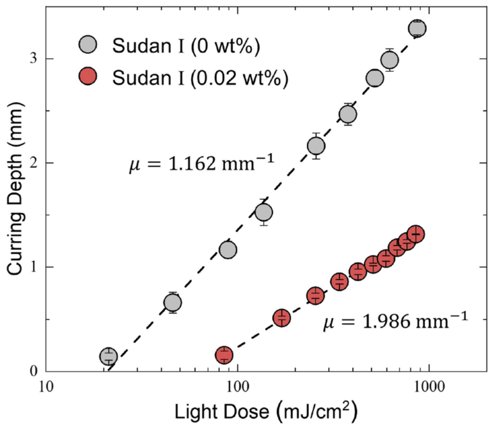

Fig. S3 Curing depth of the GMA resin with different concentrations of Sudan I (0 wt% and 0.02 wt%) as a function of light dose.

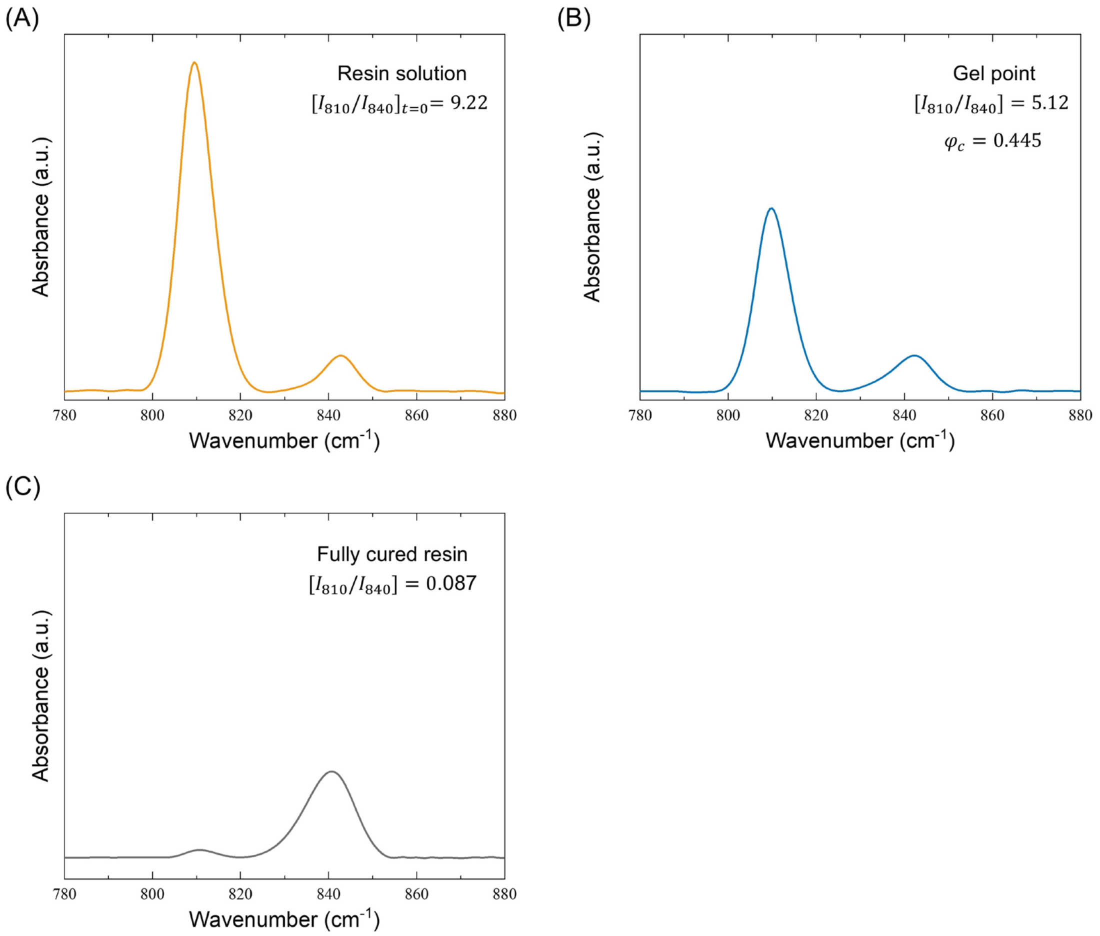

Fig. S4 FTIR analysis of GMA resin solution (A), resin at the critical gel point (B) and fully cured resin (C).

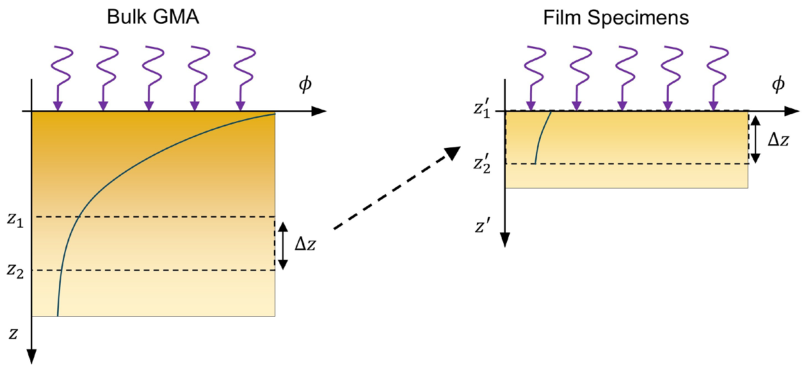

Fig. S5 Schematic illustration of the equivalent tensile test approach for determining modulus distribution in GMA.

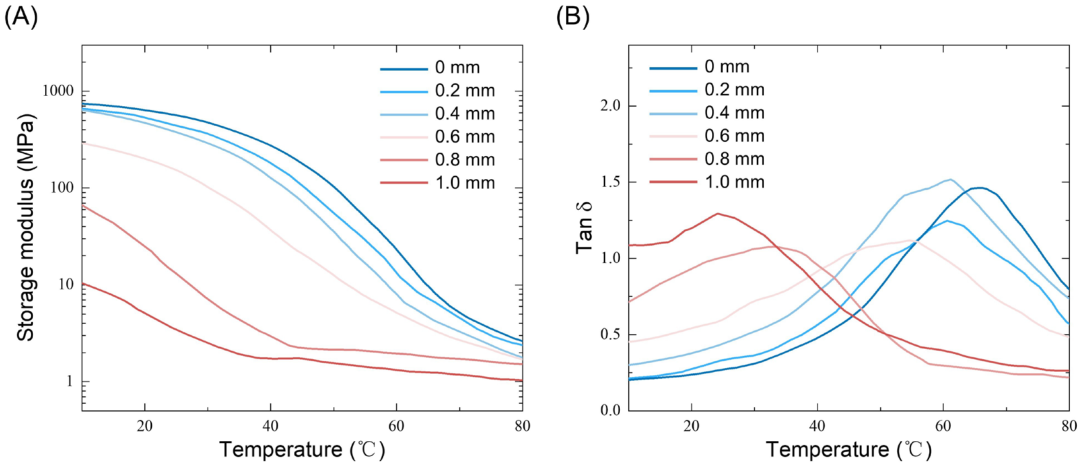

Fig. S6 (A) Storage modulus and (B) tan δ measured by DMA for 150-μm-thick films corresponding to different depths within a 1-mm-thick GMA.

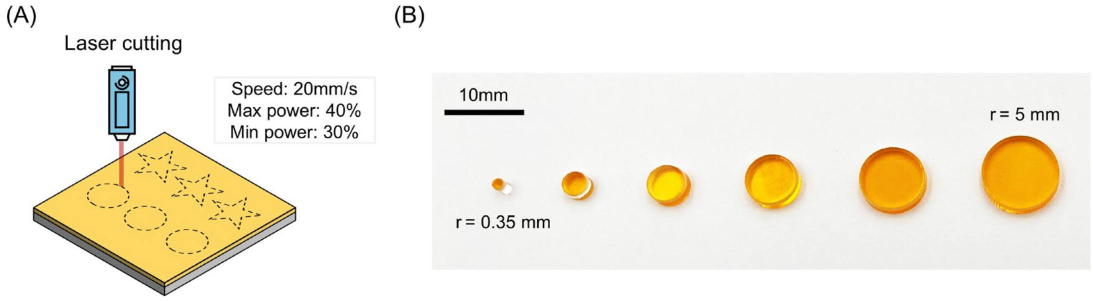

Fig. S7 Laser cutting of GMA into customized geometries. (A) Schematic illustration of laser cutting used to fabricate GMA samples with customized shapes and size. (B) Optical images of laser-cut GMA samples with different sizes and geometries, including circular samples with radii ranging from r = 0.35 mm to 5 mm. Scale bar, 10 mm.

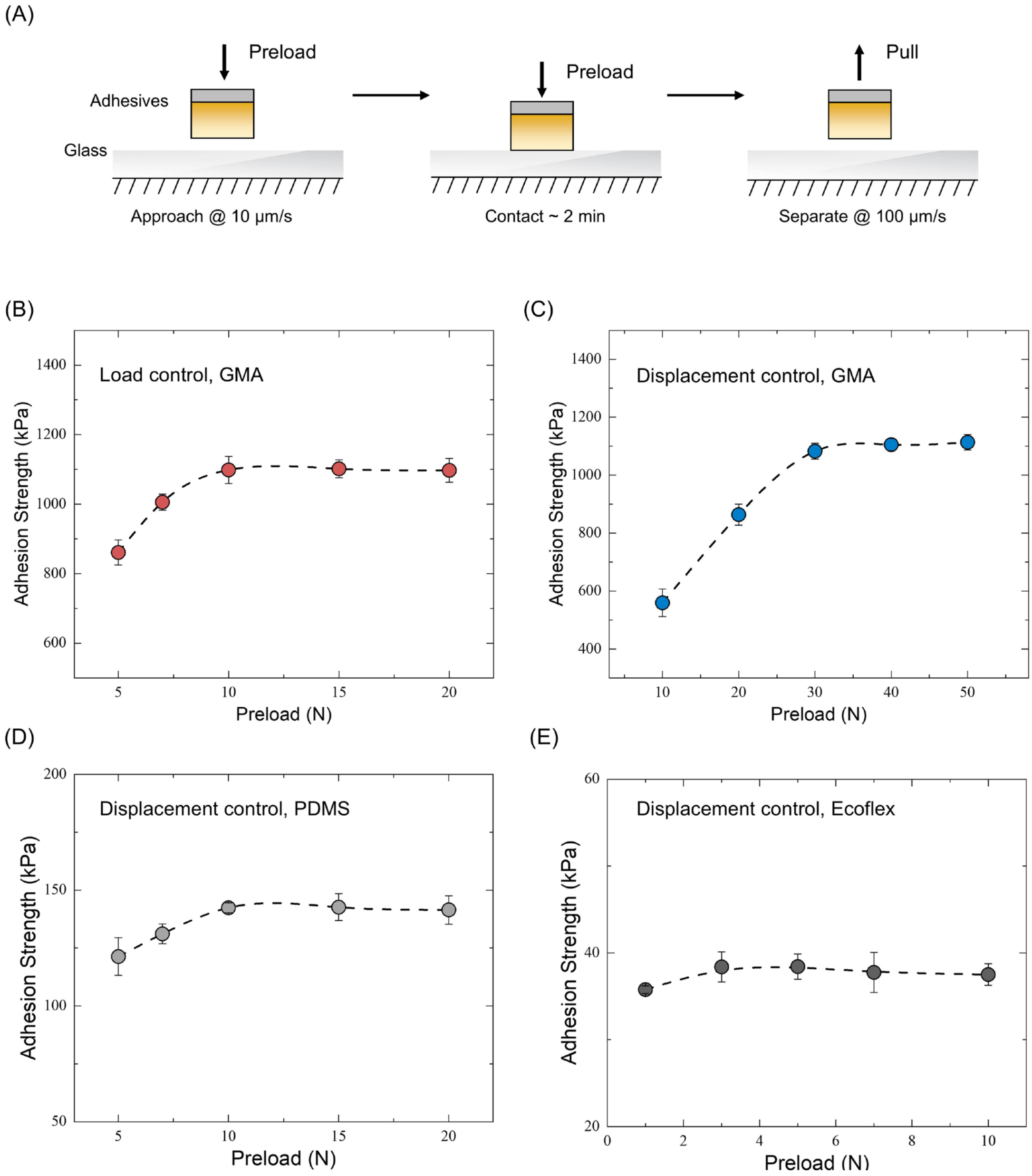

Fig. S8 Adhesion measurement procedure and preload dependence. (A) Schematic illustration of the pull-off testing protocol, including preload, dwell and separation steps. Adhesion strength of the GMA measured under load control (B) and displacement control (C) as a function of preload. (D, E) Adhesion strength measured under displacement control as a function of preload for PDMS and Ecoflex.

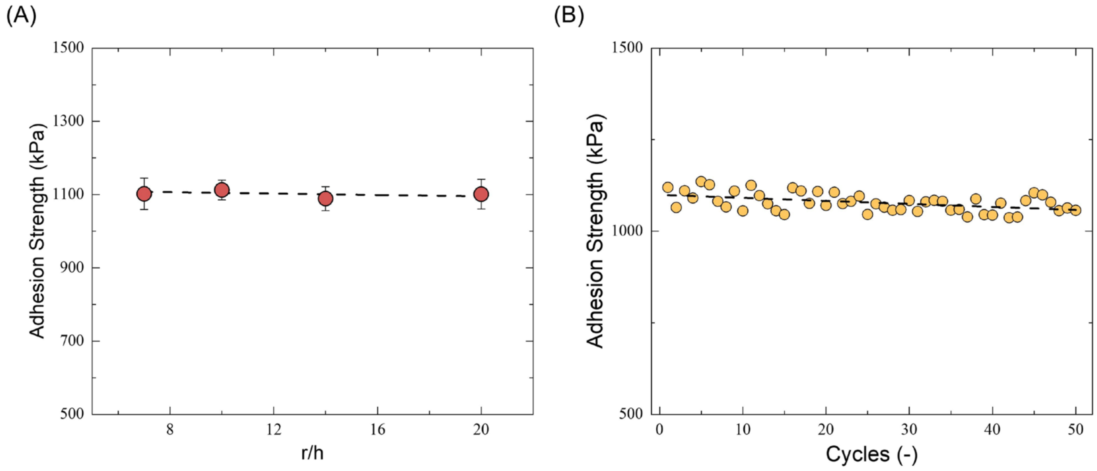

Fig. S9 Scalability and stability of GMA adhesion performance. (A) Adhesion strength of GMA samples as a function of the aspect ratio (r/h), with sample radii extended up to 20 mm. (B) Adhesion strength of a GMA sample measured over 50 loading–unloading cycles.

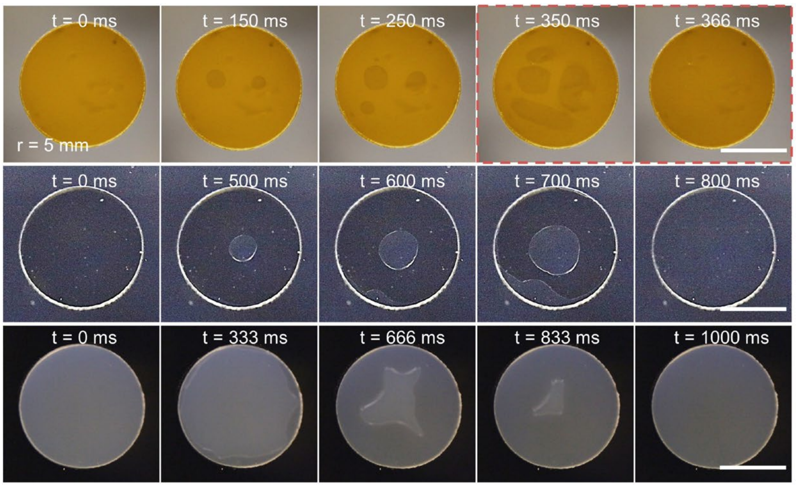

Fig. S10 Optical images capturing the detachment process of GMA, PDMS, Ecoflex samples with a radius of r = 5 mm.

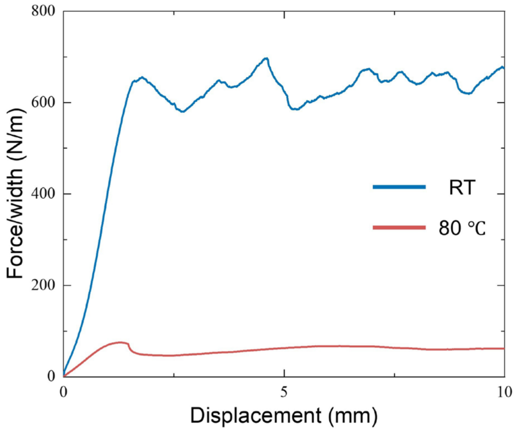

Fig. S11 Adhesion energy of the GMA at room temperature and 80 °C measured by a 90° peel test.

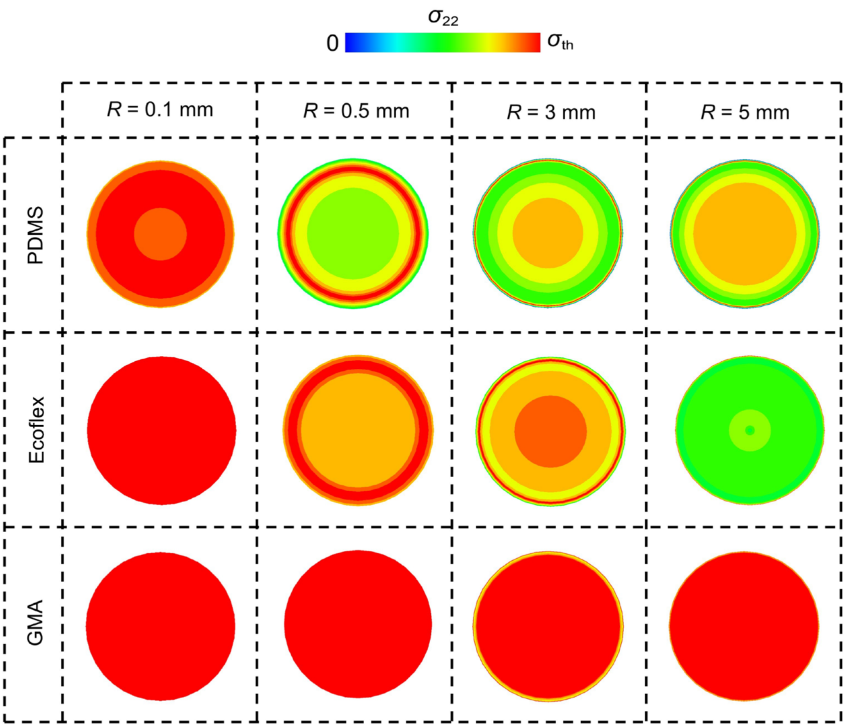

Fig. S12 FEA simulations of interfacial stress at the point of maximum force during debonding for GMA, PDMS and Ecoflex as a function of sample size.

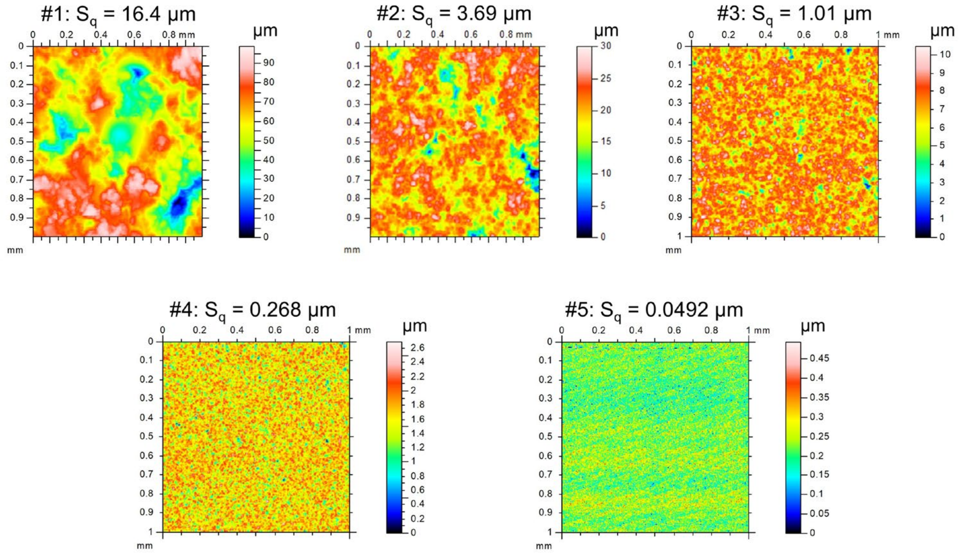

Fig. S13 Surface roughness profile of the rough glass substrate measured by a contact profiler.

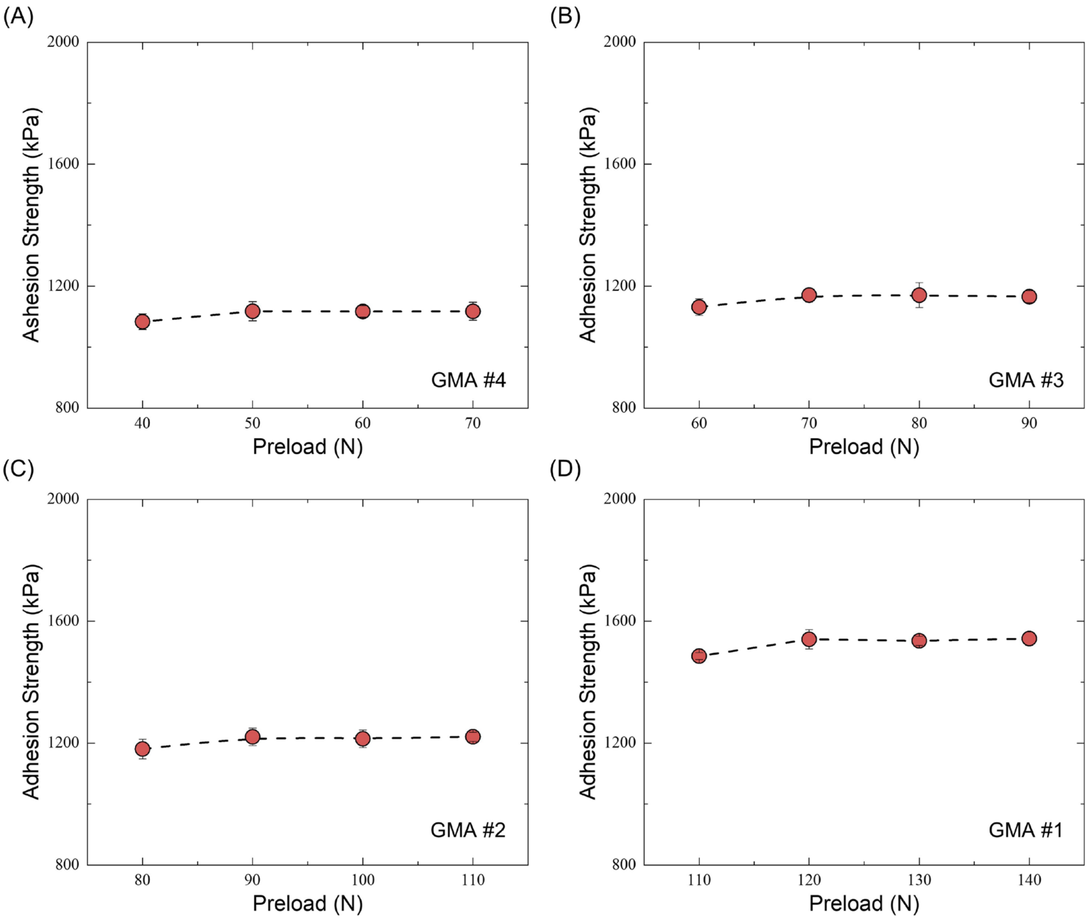

Fig. S14 Adhesion strength measured under displacement control as a function of preload for GMA on substrates with different roughness. (A) S_q = 0.268 µm. (B) S_q = 1.01 µm. (C) S_q = 3.69 µm. (D) S_q = 16.4 µm.

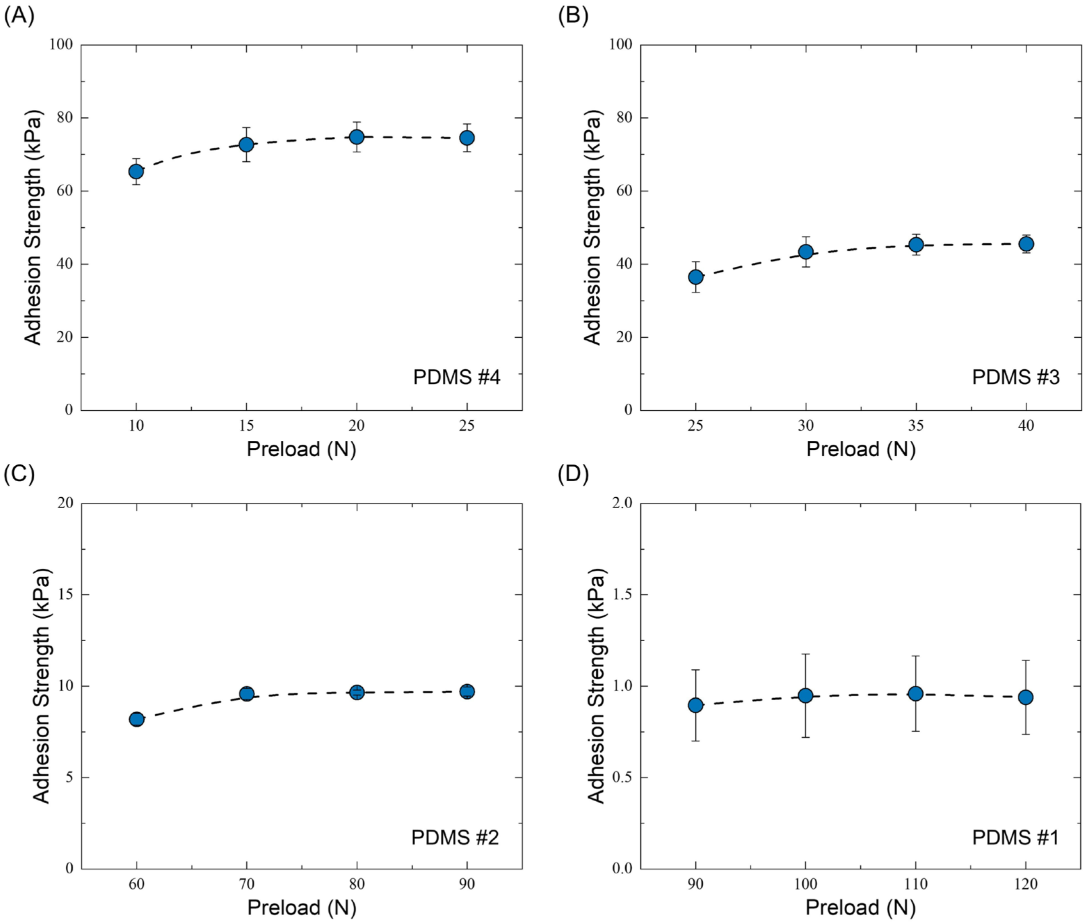

Fig. S15 Adhesion strength measured under displacement control as a function of preload for PDMS on substrates with different roughness. (A) $S_q = 0.268$ μm. (B) $S_q = 1.01$ μm. (C) $S_q = 3.69$ μm. (D) $S_q = 16.4$ μm.

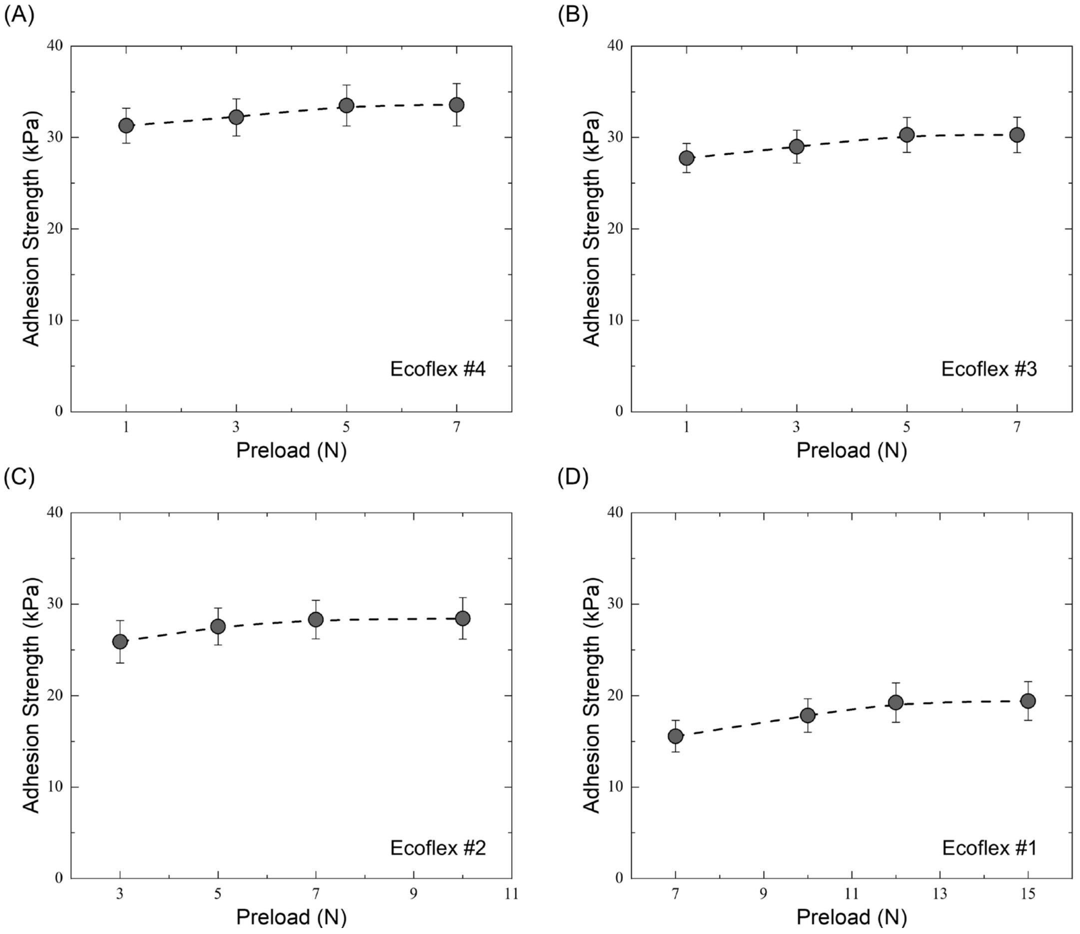

Fig. S16 Adhesion strength measured under displacement control as a function of preload for Ecoflex on substrates with different roughness. (A) $S_q = 0.268$ μm. (B) $S_q = 1.01$ μm. (C) $S_q = 3.69$ μm. (D) $S_q = 16.4$ μm.

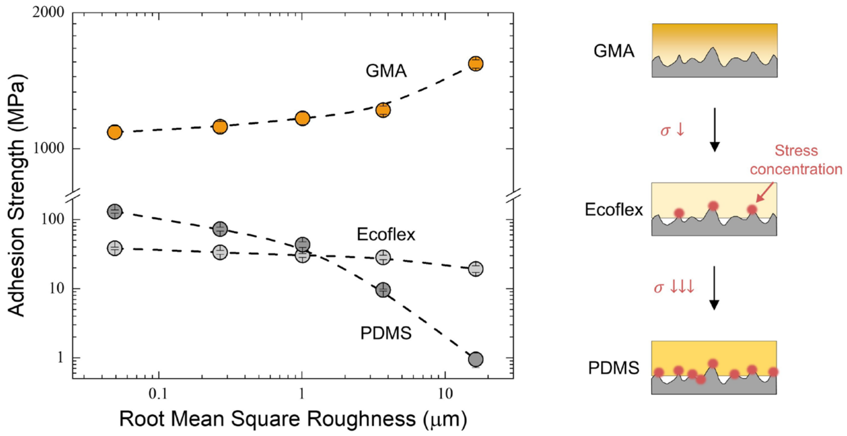

Fig. S17 Surface adaptability of GMA. (A) Adhesion strength of GMA, PDMS, and Ecoflex as functions of root mean square (RMS) surface roughness. Right panel: Schematics of the interfacial contact conditions on rough surfaces.

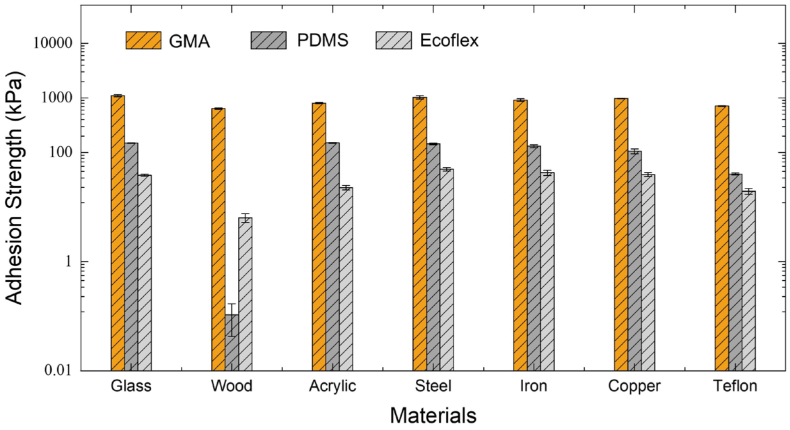

Fig. S18 Adhesion strength of GMA, PDMS, and Ecoflex on various substrates, including high-roughness (wood), low-surface-energy (Teflon), and metallic or polymeric surfaces.

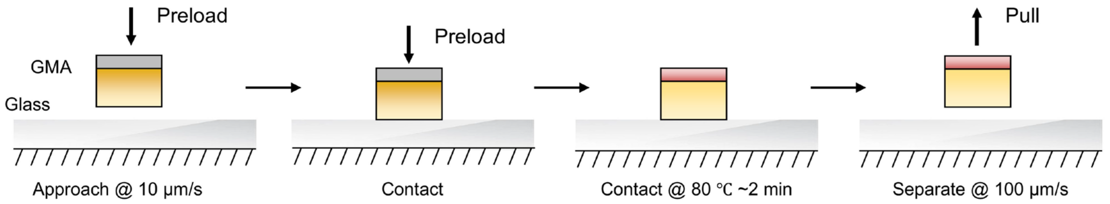

Fig. S19 Schematic illustration of the thermally switchable pull-off adhesion measurement.

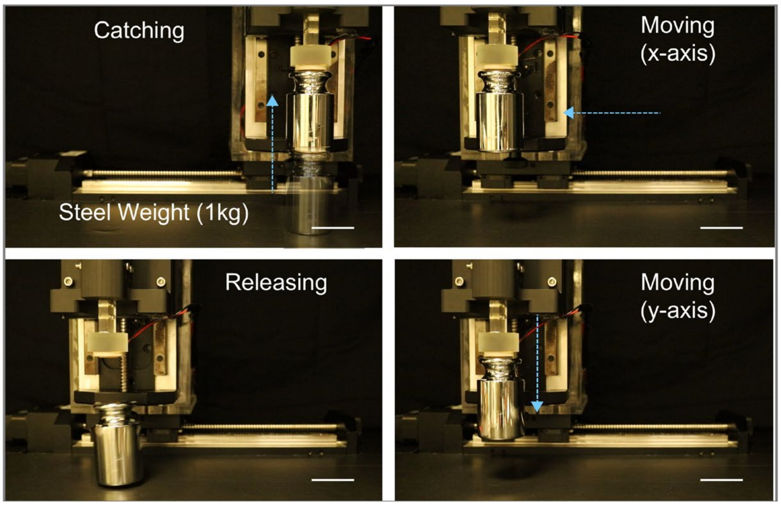

Fig. S20 Schematic illustration of a two-axis motorized system integrating a heater and GMA as a thermally switchable pick-and-place platform for manipulating a 1 kg steel weight.

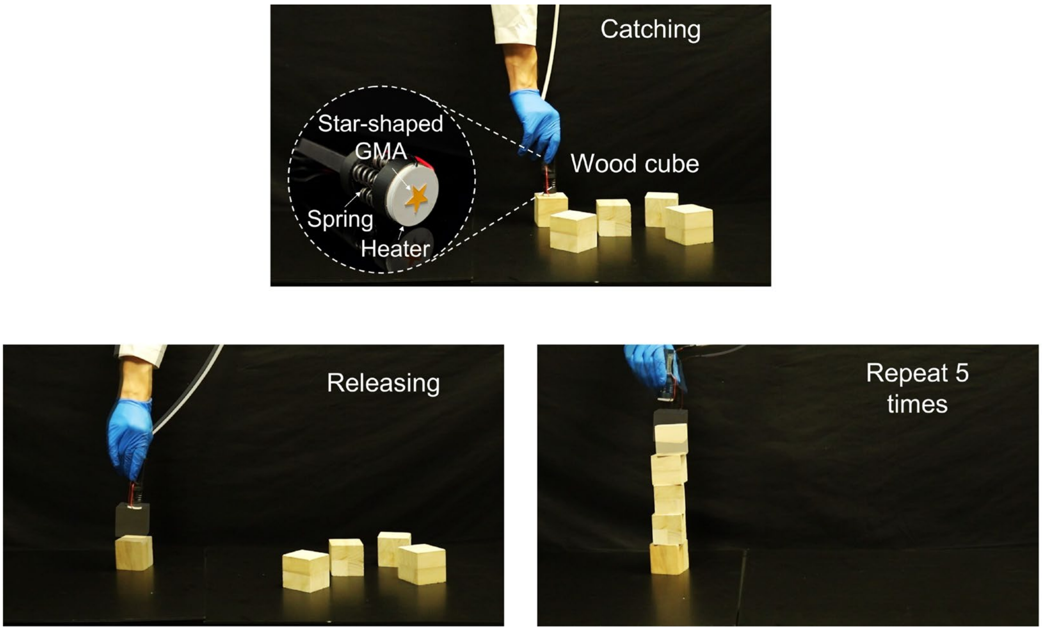

Fig. S21 Handheld pick-and-place device utilizing a star-shaped GMA for repeated capture and release of rough wooden cubes over five consecutive cycles without performance degradation

Table S1 Comparison of GMA with previously reported switchable soft adhesives in adhesion mechanisms and performance.

Materials	Mechanism description	Maximum adhesion (kPa)	Minimum adhesion (kPa)	Switchability (-)	Ref
GMA	Thermal driven transition from strong DMT-like adhesion to weak JKR-like adhesion via modulus gradient erasure	1107.40764	130.19847	8.44	This work
	Shape facilitates transition from shape-insensitive behavior and shape-sensitive behavior		72.00684	15.38	
Magnetorheological Grease	Magnetic-field–driven transition from soft conformal adhesion to stiff locked adhesion via magnetorheological stiffening	7.79	0.36	21.63888889	5
		4.51	0.7	6.442857143	
		3.94	0.55	7.163636364	
		38.98	22.25	1.751910112	
Magnetorheological Elastomer		46.67	30.03	1.554112554	6
		40.42	27.2	1.486029412	
		36.26	23.92	1.515886288	
		32.69	23.18	1.410267472	
NdFeB/PDMS	Magnetic-field–driven adhesion switching via micro-beam bending–	6.652046024	0.29882238	22.26086957	7

Composites	induced edge crack initiation	7.535520886	0.636621592	11.83673469	
Borate ester hydrogels	Electric-field–driven adhesion switching via electrolysis-induced reversible cleavage/reformation of borate esters that expose or shield catechol groups	12.28	0.25	49.12	8
		12.33	0.35	35.22857143	
		12.89	0.45	28.64444444	
		9.88	0.15	65.86666667	
Dynamic multiscale contact synergy hydrogel	Thermal-driven adhesion switching via dynamic multiscale contact synergy that couples catechol screening with modulus/roughness regulation	32	0.13	246.1538462	9
		10.86	0.51	21.29411765	
		22.43	0.59	38.01694915	
		24.26	0.84	28.88095238	
		24.42	0.3	81.4	
		18.19	0.55	33.07272727	
		20.45	0.45	45.44444444	
CNF-DA/PAA@Fe^{3+} hydrogel	UV-driven adhesion switching via photo-Fenton–mediated Fe^{3+}/Fe^{2+} coordination dynamics in cellulose nanofiber–reinforced supramolecular networks	76.176	13.1275	5.802780423	10
		65.1083	16.6132	3.919070378	
		61.1454	18.2542	3.349661996	10
		56.5292	9.58999	5.894604687	

		60.1929	11.5781	5.198858189	
		59.2553	7.22921	8.196649426	
		67.1851	14.4242	4.657804246	
		59.2553	14.6524	4.044067866	
PBA/[EMIM][NTf$_2$] ionogel	Thermal-driven adhesion switching via LCST-induced phase separation in ionogels that modulates interfacial interactions and contact area	31.75	6.46	4.914860681	11
		40.64	5.19	7.83044316	
		33.37	8.89	3.753655793	
		32.21	7.27	4.430536451	
		39.14	7.27	5.383768913	
poly (N-isopropylacrylamide hydrogel	Thermal-driven adhesion switching via LCST-induced phase separation of PNIPAm hydrogels that retract interfacial chains and expel water	87.19	0.58	150.3275862	12
		86.92	1.22	71.24590164	
		67.24	0.74	90.86486486	
		88.68	0.53	167.3207547	
		39.34	2.82	13.95035461	
Silicon Rubber	Preload-driven adhesion switching via underside buckling that reduces effective contact under high compressive load	34.1906	0.288209	118.6312711	13
		54.9599	0.589378	93.25068123	
		74.7514	1.50999	49.50456626	

		88.4398	3.36521	26.28061845	
		97.0115	6.49974	14.92544317	
		104.303	7.39495	14.10462545	
		109.037	8.61051	12.66324527	
Shape memory polymer (SMP)		96.5909	43.6688	2.211897281	14
		96.2662	0.811688	118.6000039	
TGMM/AAMM copolymer	Light-driven adhesion switching via azobenzene photoisomerization that modulates modulus, polarity, and interfacial interactions	1231.61	1028.83	1.197097674	15
		1076.54	832.008	1.293905828	
		861.829	685.885	1.256521137	
		766.402	590.457	1.297981055	

Table S2 Benchmarking of GMA against commercial 1-mm-thick double-sided tapes across five key performance metrics. Adhesion strength was evaluated on PTFE and rough glass surfaces (RMS = 16.4 μm), shape-effect ratio ($\sigma_{star}/\sigma_{round}$), adhesion switchability, and adhesion durability. GMA exhibited superior performance in all categories compared to commercial tapes, demonstrating its advantages on low-surface-energy and rough surfaces, in geometric adaptability, tunable adhesion, and long-term durability.

Tapes	Adhesion on PTFE surface (kPa)	Adhesion on rough wood surface (kPa)	Shape-effect ratio (-)	Adhesion switchability (-)	Adhesion lifetime (min)
GMA	710.42	635.12089	1.00711	15.38	62.4
3M Scotch STD-19	251.20654	369.97877	0.5351	1	0.06
3M VHB 4910	264.7411	440.73924	0.64894	1	0.19
3M Scotch 419	221.21873	300.80798	0.64593	1	0.06333
Polar Bea FP-1902	212.8924	308.53299	0.70113	1	0.06667

References

1. Vitale, A. et al. Interfacial Profile and Propagation of Frontal Photopolymerization Waves. *Macromolecules* **2014,** *48*, 198-205.

2. Yue, L. et al. Single-vat single-cure grayscale digital light processing 3D printing of materials with large property difference and high stretchability. *Nature Communications* **2023,** *14*, 1251.

3. Kuang, X. et al. Grayscale digital light processing 3D printing for highly functionally graded materials. *Science Advances* **2019,** *5*, eaav5790.

4. Darby, D. R. et al. Modulus and adhesion of Sylgard 184, Solaris, and Ecoflex 00-30 silicone elastomers with varied mixing ratios. *Journal of Applied Polymer Science* **2022,** *139*, e52412.

5. Wang, D. et al. Sensing-triggered stiffness-tunable smart adhesives. *Science Advances* **2023,** *9*, eadf4051.

6. Min, H. et al. Stiffness-tunable velvet worm–inspired soft adhesive robot. *Science Advances* **2024,** *10*, eadp8260.

7. Zhao, J. et al. Smart Adhesives via Magnetic Actuation. *Adv Mater* **2022,** *34*, e2107748.

8. Huang, J. et al. Electrically programmable adhesive hydrogels for climbing robots. *Science Robotics* **2021,** *6*, eabe1858.

9. Zhang, Z. et al. Design of large-span stick-slip freely switchable hydrogels via dynamic multiscale contact synergy. *Nat Commun* **2022,** *13*, 6964.

10. Zhang, L. et al. Cellulose nanofiber-mediated manifold dynamic synergy enabling adhesive and photo-detachable hydrogel for self-powered E-skin. *Nat Commun* **2024,** *15*, 3859.

11. Wang, S. et al. Enhancing Grasping Function with a Thermoresponsive Ionogel Adhesive Glove for Patients with Rheumatic Diseases. *Adv Sci* **2025**, e2414761.

12. Yin, Q. et al. Highly switchable and reversible soft sticky adhesives based on thermo-responsive phase separation. *Extreme Mechanics Letters* **2025,** *75*, 102293.

13. Tu, C. et al. Preload-Induced Switchable Adhesion. *Small* **2024,** *20*, e2305091.

14. Linghu, C. et al. Fibrillar adhesives with unprecedented adhesion strength,

switchability and scalability. *National Science Review* **2024,** *11*, nwae106, .

15. Oh, M. et al. Eco-friendly and photo-switchable smart adhesives from biomass-based copolymers with acid azobenzene functions. *Chemical Engineering Journal* **2025,** *520*, 166035.